

## Jue Wang

Shanghai Key Laboratory of Digital Manufacture  
for Thin-Walled Structures, and State Key  
Laboratory of Mechanical System and Vibration,  
Shanghai Jiao Tong University,  
Shanghai 200240, China  
e-mail: wangjue1995@sjtu.edu.cn

## Genliang Chen

Shanghai Key Laboratory of Digital Manufacture  
for Thin-Walled Structures, and State Key  
Laboratory of Mechanical System and Vibration,  
Shanghai Jiao Tong University,  
Shanghai 200240, China  
e-mail: leungchan@sjtu.edu.cn

## Zhuang Zhang

Shanghai Key Laboratory of Digital Manufacture  
for Thin-Walled Structures, and State Key  
Laboratory of Mechanical System and Vibration,  
Shanghai Jiao Tong University,  
Shanghai 200240, China  
e-mail: z.zhang@sjtu.edu.cn

## Jiaqi Suo

Gensler,  
Baltimore, MD 21202  
e-mail: suoqiaqi0710@gmail.com

## Hao Wang

Shanghai Key Laboratory of Digital Manufacture  
for Thin-Walled Structures, and State Key  
Laboratory of Mechanical System and Vibration,  
Shanghai Jiao Tong University,  
Shanghai 200240, China  
e-mail: wanghao@sjtu.edu.cn

# Wireless Multiplexing Control Based on Magnetic Coupling Resonance and Its Applications in Robot

*Nowadays, more and more researchers are pursuing miniaturized and lightweight structure of robots. However, robots with multiple actuators require large control systems if each actuator needs to be controlled independently. In addition, the cables and circuits for control and power supply are the obstacles in reducing size and weight. In this article, a wireless multiplexing control system based on magnetic coupling resonance (MCR) is proposed. The control system can realize wireless energy transmission and control simultaneously. By decomposing a composite signal, it can control multiple actuators with only one input signal. However, in previous researches, their applications are primary and simple due to the switch control without feedback and the lack of systematic design method for robot application. Thus, based on the discrete form of composite signal, the closed-loop of wireless multiplexing control is presented, which makes this promising method a step closer to the practical application. Besides, based on the theoretical model of load power and transmission efficiency, five parameters to be optimized are extracted in accordance with the actual design requirements. The optimization algorithm for load power is proposed using particle swarm optimization (PSO). As for its applications in robots, a Delta robot with flexible linkage and an untethered multidrive pipe robot for sampling operation are designed to demonstrate the proposed control method. The experiment results of the Delta robot show the reliability and accuracy of the system, while the results of the pipe robot prove its potential use in the untethered robot system.*

[DOI: 10.1115/1.4051357]

**Keywords:** magnetic coupling resonance, multiplexing control, optimization algorithm, parallel robot, pipe robot

## 1 Introduction

Modern robots originated in the middle of the 20th century. With the progress of science and technology, robots are gradually applied to all parts of life to reduce costs and improve efficiency. The abundant types and diversified functions of robots require more and more complex structures. Meanwhile, miniaturization and lightweight have become the main trend of robot development [1].

However, with the development of robotics, the number of actuators in a robot system is increasing to meet the requirement of more complicated tasks. Aiming to control each actuator independently, traditional single-input single-output control will inevitably lead to larger control system. Thus, the multiplexing control becoming a promising way to deal with this problem. Here, multiplexing is basically a concept in telecommunications and computer networks, which means that several outputs may be carried using one wire. In a broad sense, when the output of a system is larger than the number of input signal just because of the multi-use of the input or the input signal contains multiple information, it can be regarded as multiplexing control or single-input multioutput (SIMO) control. For example, the programmable surface, a typical multi-actuator system, often requires large space for the control system, such as INFORM proposed by Follmer et al. [2] and relief 3D display

system designed by Leithinger and Ishii [3]. As for multiplexing control, it can effectively reduce the volume of the controllers and cables, which can be a reliable method to realize miniaturization and lightweight of the robot system.

Besides, the cables and circuits of the robot system are also the obstacles for miniaturizing industrial robots, soft robots, and micro-robots. Even if the wireless control can be realized, wired power supply or battery takes up a lot of space and weight. Especially for soft robots, the dragging cable often affects their motion characteristics. Besides, when using the battery, its endurance also limits the application environment.

To solve the aforementioned problems simultaneously, driving the robot system by magnetic field can be a feasible way since the frequency characteristic of magnetic field is the basis of frequency-division multiplexing and it can also transfer energy wirelessly. Magnetic-driven robots usually include two different types. One is to use the gradient of strong magnetic field as power or use the rotation and vibration of magnetic field to make the microrobot rotate or swing. This method is mostly used to operate the micro-cluster-robot, which is difficult to control the motion of single actuator or robot individually [4–8]. Johnson et al. [9] proposed a new localized magnetic field generating system to control microrobots independently, but it is selective control rather than the multiplexing control since different microrobots cannot be controlled simultaneously.

Another category is magnetic coupling resonance (MCR) whose frequency selective characteristic can be fully utilized. However, before the mid-range and high-power wireless charging technology,

Contributed by the Mechanisms and Robotics Committee of ASME for publication in the JOURNAL OF MECHANISMS AND ROBOTICS. Manuscript received February 12, 2021; final manuscript received May 18, 2021; published online July 13, 2021. Assoc. Editor: David J. Cappelleri.

which was based on strong MCR, was first proposed by Kurs et al. [10] in 2007, the MCR was widely applied for microrobots due to the energy limitation. For example, Kratochvil et al. [11–13] proposed a kind of microrobots driven by MCR, which can drive a unit independently according to the magnetic field frequency under a special substrate. While on the basis of MCR, Xu and Liu [14] transformed the vibration of the soft magnet into a rotating output, which achieved the transition and rotation of micro-actuator. Besides, Tung et al. [15] put forward a kind of microrobot based on MCR named PolyMite. It used Su-8 polymer as a surface material, which can make the robot speed up to 20 mm/s when driven in air. Its multiple degree-of-freedom motion shows the ability to transport small objects in water.

After implementing the LC coils, multiple actuators, such as micromotor [16], shape memory alloy (SMA) [17–19], and electric heating device [20], can be driven since sufficient energy can be transferred based on such wireless power transfer (WPT) system. Its longer transmission distance and higher transmission energy [21] provide a stage for various actuator mechanisms of soft robot. Besides, the characteristics of frequency selectivity has a potential to achieve multiplexing control for regular actuator mechanisms [22]. When a composite signal is applied as input, the energy can be selectively transmitted by controlling the frequency through the band-pass effect of LC coils.

Since the MCR based on WPT can not only achieve multiplexing control for multi-actuator system but also be used to drive diverse actuators based on its characteristics of energy transmission, it is a promising method for controlling robot system, especially the programmable surface and artificial skin, which possess large numbers of actuators. As to the previous researches in this field, Ali et al. [17–19] proposed a method based on the magnetic coupling resonance to control heating of three SMAs. When inputting one composite signal with three different frequencies, three SMA actuators can be controlled simultaneously and independently. Mc Caffrey et al. [23] proposed a continuum robotic caterpillar based on the same system, locomotion of the robot achieved by driving the SMA actuators sequentially by sweeping the input signal in a certain increment. Boyvat et al. [24] proposed that magnetic coupling resonance can bring a rich variety of features concerning forces and torques to the cells, which can lead to the wirelessly powered motor. After that, Boyvat et al. [25] used this principle to heat SMA with magnetic coupling resonance to realize a three-drive origami mechanism and wireless soft actuators [20]. Yu et al. [26] applied magnetic coupling resonance technology to e-skin, driving the vibration unit on the e-skin to generate tactile sensation.

However, considering these close relevant researches, some of the initial works only focused on the analysis of frequency selectivity rather than providing a practical application. Besides, achieving on/off switch control without feedback can be applied to only primary robot applications. For example, in Boyvat et al.'s [20,25] and Mc Caffrey et al.'s [23] works, the robot based on this method can only achieve bending and grabbing or simple locomotion without any precision. Therefore, there is still a gap between this promising method and practical robot application. Besides, many researchers have carried out in-depth research on its theoretical modeling [22,27–29]. But for robot application, there is no corresponding systematic method including theoretical modeling of magnetic coupling resonance and optimization of circuit modeling to support the system design.

In this article, a wireless multiplexing control system is proposed based on MCR. This control system can realize the wireless energy transmission and control simultaneously. By decomposing a composite signal, it can control multiple actuators only with one input signal. Based on the discrete form of composite signal, the closed-loop control of the aforementioned method is presented, which is able to bring such control method from primary application to advanced application. To provide a systematic design method for robot application, in accordance with the actual design requirements, five parameters to be optimized are extracted based on the

theoretical model of load power and transmission efficiency. Then by using particle swarm optimization (PSO), the optimization algorithm for load power is proposed. As for its application, a Delta robot with flexible linkage and an untethered pipe robot with four different motion forms are designed to validate the control method. The experiment results show that the advanced application of such control method is achieved successfully since the accurate multiple degrees-of-freedom motion of the Delta robot with feedback can be realized. Besides, compared with relevant research, various motion forms of the untethered robots are achieved to complete the certain assignments, which shows a great improvement before this method can be fully applied in practical robot application.

## 2 The Principle of Wireless Multiplexing Control

**2.1 The Frame of Wireless Multiplexing Control.** As shown in Fig. 1, the whole system includes two parts: the transmitting part and receiving part. On the transmitting side, the signal generator produces the AC signal and the inverter, such as full-bridge inverter and half-bridge inverter, adds the power of DC voltage to the AC signal, which can make the LC coil in the transmitting side generate sufficient electromagnetic energy. Here, the natural frequency of transmitting and receiving LC coil should be the same, so that the energy is transferred by magnetic coupling resonance not the electromagnetic induction. After the LC coil in the receiving side received the energy, to provide a steady DC voltage to the robotic system, the received AC energy is rectified by a full-bridge rectifier and then regulated by a linear regulator.

**2.2 The Principle of Close-Loop Multiplexing Control.** The LC oscillation circuit itself has a natural resonance frequency, so when the composite signal is input, the LC coil itself can be seen as a band-pass filter, and under ideal conditions, only natural resonance frequency signal will be induced. By using this feature, when a composite signal is an input to multiple LC coils with different resonance frequencies at the same time, theoretically, each LC coil will only sense the same components as its own natural frequency. As shown in Fig. 1, if the natural frequency of each LC coil in the receiving part is different, the receiving LC coil can only get the energy when the input composite signal has its natural frequency component. Therefore, a single composite signal can be used to control multiple independent outputs. This is the realization principle of SIMO control based on MCR.

In the aspect of signal input, to achieve the multiplexing control, the signal must contain a variety of different information, so the input signal needs to be a multifrequency composite signal. In an ideal state, the magnitude of the LC coil sensed is directly proportional to the amplitude in the frequency domain Fourier transform. There are two forms of composite signal. As shown in Fig. 2(a), the

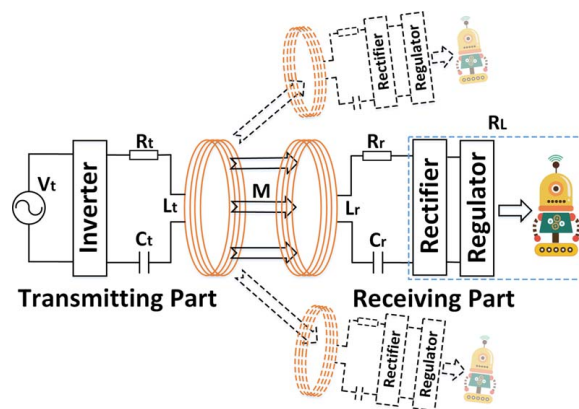


Fig. 1 The frame of the wireless multidrive control

first is direct composite, that is, only through the Fourier transform can the frequency information inside the signal be extracted. The second is the discrete form of composite signal shown in Fig. 2(b), which means the signals of different frequencies are combined and each frequency takes up a part of the total period separately.

As for the discrete composite signal, when  $\Delta t_1$ ,  $\Delta t_2$ , and  $\Delta t_3$  are relatively small, due to the hysteresis effect, it can produce the same effect as the normal composite signal. Here, three different frequencies  $f_1$ ,  $f_2$ , and  $f_3$  are for different outputs. Besides, this kind of signal is not only suitable for MCU or controller to generate but also convenient for feedback control. Therefore, this signal is selected as input in the following applications.

For general square wave signal, adjusting pulse width modulation (PWM) according to the feedback signal is the most common method, while for discrete composite signal, its feedback control can be realized in the following forms. As shown in the right side of Fig. 2(b), by dividing the  $\Delta t_i$  into two parts: one is full output and the other is no-load output. The intensity of each frequency component can be controlled by adjusting the proportion of full output ratio, that is,  $\gamma_1$ ,  $\gamma_2$ , and  $\gamma_3$ . Here,  $\gamma_i$  can be used as the input parameter in PID control just like the duty cycle in PWM.

### 3 Modeling and Parameter Optimization

In the circuit of magnetic coupling resonance shown in Fig. 1, the natural frequency of LC coils can be calculated by following equation:

$$f = \frac{1}{2\pi\sqrt{LC}} \quad (1)$$

Thus, to have the same resonance frequency of transmitting and receiving part, there should be  $L_t = L_r = L$  and  $C_t = C_r = C$ . When evaluating the performance of circuit, the most significant parameters are load power and transmission efficiency. Based on the Kirchhoff's circuit laws, the mathematical model of load power and transmission efficiency can be derived as follows:

$$P_{in} = \frac{V_i^2(R + R_L)}{R(R + R_L) + 4\pi^2 f^2 M^2} \quad (2)$$

$$P_L = \frac{4\pi^2 f^2 M^2 V_i^2 R_L}{[R(R + R_L) + 4\pi^2 f^2 M^2]^2} \quad (3)$$

$$\eta = \frac{4\pi^2 f^2 M^2 R_L}{(R + R_L)[R(R + R_L) + 4\pi^2 f^2 M^2]} \quad (4)$$

where  $P_L$  and  $\eta$  are load power and transmission efficiency, respectively,  $f$  refers to the resonance frequency, and  $M$  is the mutual inductance between two coils. The root mean square value of the input signal amplitude is expressed in  $V_i$ .  $R_L$  and  $R$  are the load and circuit resistance, respectively, where the calculation is simplified by mean of setting  $R_t = R_r = R$ . Since such derivation is based on the basic circuit theory and out of the scope of this article, the detailed process is not shown here.

In the calculation of coil mutual inductance, if the number of turns  $n$  and radius  $r$  of two coils are the same and the distance between two coils is  $d$ , we have [31]

$$M = \frac{\mu_0 N^2 r}{b} [(2 - b^2)K(b) - 2E(b)] \quad (5)$$

where

$$b = \sqrt{\frac{4r^2}{4r^2 + d^2}} \quad (6)$$

where  $K(b) = \int_0^{\pi/2} \frac{d\theta}{\sqrt{1 - b^2 \sin^2 \theta}}$  and  $E(b) = \int_0^{\pi/2} \sqrt{1 - b^2 \sin^2 \theta} d\theta$  are the first and second kind of complete elliptic integral, respectively.

Based on the aforementioned equations, it can be concluded that five external parameters affect the load power and transmission efficiency, which are resonance frequency  $f$ , load resistance  $R_L$ , coil distance  $d$ , coil turns  $n$ , and coil radius  $R$ . After getting these parameters, corresponding inductance and capacitance can be derived. Since all the curves that show the relationship between system parameters with the load power have an extreme point, the results must be convergent when optimizing such parameters with the load power as an objective function.

When optimizing these parameters, some of them should be set previously based on the application requirement. For example, when the optimization target is the LC coil, the parameters related to coil including  $N$ ,  $r$ , and  $d$  need to be optimized, while the  $R_L$  and  $f$  should be known. As for the application of robots, the actuators and structure of the robot need to be determined in advance, so the load, coil radius, and coil distance are known parameters. Besides, if it is necessary to drive multiple actuators simultaneously according to its frequency selectivity, the resonance frequency also needs to be determined first. At this time, the only parameter to be optimized is the number of coil turns.

In this article, PSO algorithm [32] is used to optimize the aforementioned parameters with the load power as the adaptive value. It has the following two advantages: the first is fast convergence speed and the second is that the result is less affected by the dimension of parameters to be optimized. Before using PSO algorithm, some typical optimization algorithms, such as gradient descent method and Newton method, have been tested, but their convergence speed was slow as well as their complexity of the calculation is high. The most important thing is that when the parameter dimension is high, they may not converge. Especially for the problem stated in this article, there are five parameters to be optimized. For different application requirements, the known conditions and unknown parameters to be optimized are not the same. Therefore, PSO algorithm that has small influence on dimension and fast convergence speed is more suited.

Taking a practical optimization example, when optimizing the LC coil, after setting the power supply voltage of the transmitter to 12 V, resonance frequency to 60 kHz, load to 5  $\Omega$ , and circuit resistance to 2  $\Omega$ , the optimized parameters are coil turns, coil radius, and coil distance. Here, the particle dimension is set to 3. After the calculation in MATLAB, the optimal particle is [14.4, 42.6, 56.0]. That is, the number of turns of the coil is  $n = 14$  turns, the coil radius is  $r = 42.6$  mm, and the coil distance is  $d = 56.0$  mm. The change of the optimal value is shown in Fig. 3. The optimal solution is reached when the number of iterations is about 6, which proves that this method can converge to the optimal value quickly. Here, the final optimal load power is about 5.45 W shown in Fig. 3. The input power and transmission efficiency are 35.7% and 36.0 W, respectively, which are calculated by Eqs. (3) and (4). In this example, the load power can meet the requirement of micromotors, cameras, and most of electric-driven soft actuators, while the input power is only 36.0 W and the frequency is not high, which means that the coils in both sides will not have the heating problem. Based on the practical experiments, the heating problem only occurs in the inverter of the transmitting part, which cannot affect the practical application of robots.

### 4 Application in Robot

**4.1 Delta Robot With Compliant Joints.** The first application is the Delta robot with compliant joints. The Delta robot that requires three input motors to drive is a typical multidrive system. In this article, a delta robot in desktop level with size of 50 mm is designed, which has the potential use as the mini handle of medical robot or games console. To minimize the size and weight, laminated flexible linkages and origami structure inspired by these works [1,33,34] are used for it.



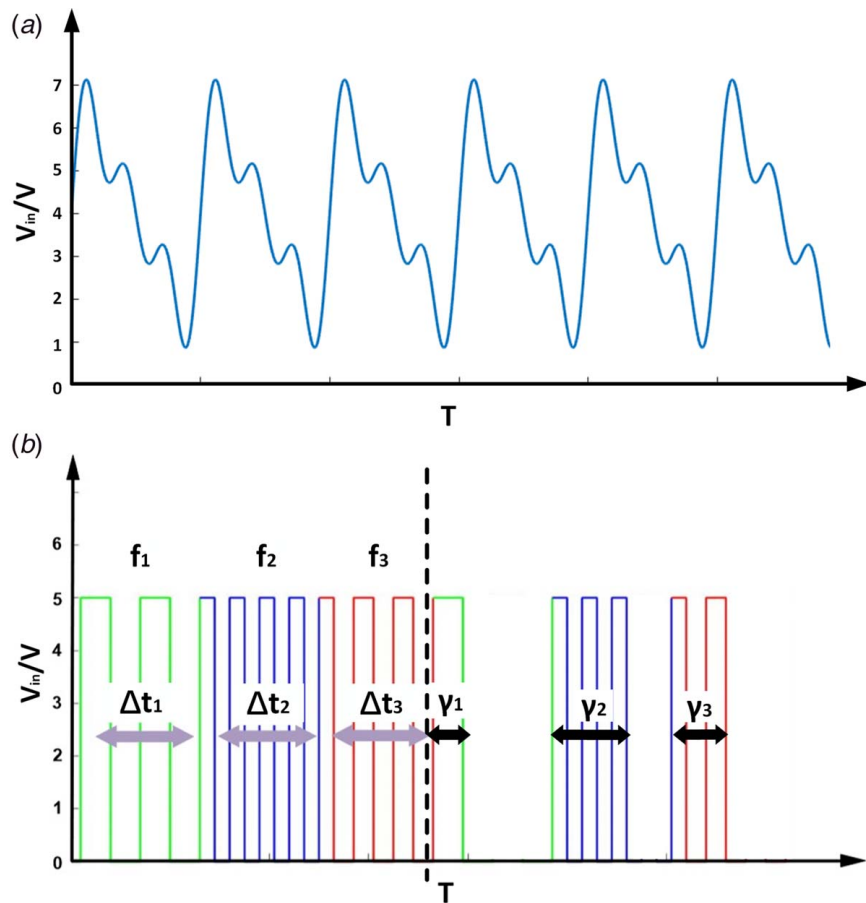


Fig. 2 Two forms of input composite signal

To verify the multiplexing closed-loop control with certain accuracy by MCR, the delta robot is an appropriate application. First, the delta robot is a kind of multi-actuator mechanism (3 actuators). Hence, the multiplexing characteristic can be proved (1 composite signal control 3 actuator simultaneously). Second, compared with previous researches, the delta robot is a kind of advanced application, since the on/off switch control (only controlling two status of actuators) cannot let delta robot move along specific trajectories. In other words, the delta robot is able to bring such control method from primary application to advanced application.

**4.1.1 The Circuit Parameters for Delta Robot.** As the input signal generator is Arduino, which can only produce signal up to 72 kHz, the range of input signal is from 10 kHz to 72 kHz. In addition, the influence of the half-frequency resonance should be avoided, after testing, the natural frequency of LC coils is determined to be 10 kHz, 28 kHz, and 40 kHz. After determining the resonant frequency, the other necessary parameters presented in Table 1 can be derived from the optimization algorithm mentioned earlier.

Then, the motion of three motors driven by different frequencies is analyzed. Figure 4(a) shows that the voltage input to the motor (the AC voltage on the receiving coil is converted to DC voltage at both ends of the motor after full-bridge rectification and motor drive) successfully avoids the half-frequency interference. The relationship between output power and frequency is plotted in Fig. 4(b). A small peak at the 20 kHz can be found just because of the half-frequency resonance. Here, the motor will start working above a certain voltage, so the decoupled motor speed-frequency curve shown in Fig. 4(c) can be derived.

**4.1.2 The Overall Scheme of Delta Robot.** The overall schematic diagram of the system is shown in Fig. 5. According to

different trajectories, the inverse kinematics of the calculator in MATLAB is first transformed into C code and imported into the Arduino 2560. The square wave signal is generated by Arduino 2560 and input to the transmitting coil after amplified by half-bridge inverter circuit. In the delta robot system, there is also a STM32 MCU used for the collection of motor encoder signal and the communication with Arduino 2560. To ensure the wireless characteristics of the whole system, the communication mode is Bluetooth. Two HD cameras next to the robot system is used to collect the moving images of the end-effector of robot and finally uses MATLAB to process them.

Delta robot system is shown in Fig. 6, in which the upper figure is the digital model of the whole system, and the lower figure shows the internal structure of the receiving and transmitting part. It can be seen from the figure that the whole system is divided into the following parts: transmitting part, receiving part, delta robot with flexible linkages, camera 1 and 2, and feedback control circuit. There are four pairs of LC coils in the system, three of which are used to control the three input motors of delta robot, and the other pair of coils are used to control the power supply of MCU at the receiving end, which can ensure the complete separation between the receiving end and the transmitting end.

The micro motor of the delta robot we choose is a hollow cup motor (made by FAULHABER), which is equipped with a 1:50 reducer and an integrated encoder. The length and the width of it are 32 mm and 8 mm, respectively, and the output is a gear with width 2.9 mm.

The half-bridge inverter amplifier circuit mainly consists of two parts, which are control and drive circuit for MOSFET. The core component of the control circuit is ADUM3223 (isolated half-bridge gate driver), which can provide 3000 V isolation. According to the principle of half-bridge inverter, two signals of different

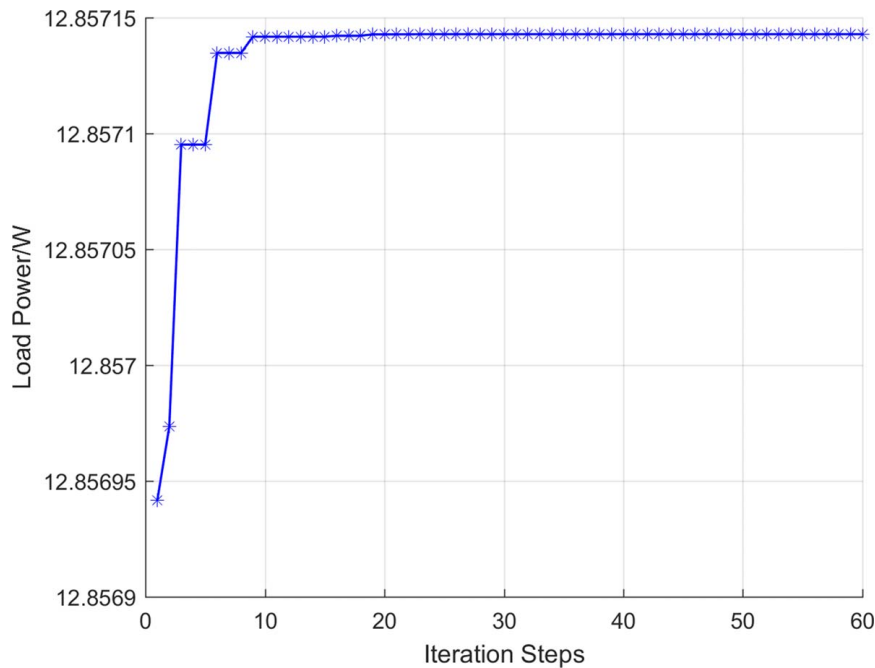


Fig. 3 The curve of optimal value change in circuit system optimal design

Table 1 Circuit parameter table for delta robot

Coil turns	Inductance (H)	Capacitance (T)	Resonance frequency (Hz)
55	$1.38 \times 10^{-4}$	$1.84 \times 10^{-6}$	10,000
34	$5.27 \times 10^{-5}$	$7.11 \times 10^{-7}$	26,000
28	$3.57 \times 10^{-5}$	$4.43 \times 10^{-7}$	40,000

phases are needed for the circuit, so the SN74LS04N (six-bit inverter) is added in the control circuit, which can convert the one input signal into two inverted signals. IRF640 is used as MOSFET transistor of half-bridge inverter circuit. This kind of transistor can withstand 200V voltage and 18A current with n-channel transistor polarity, and the maximum power consumption is 150W, which can fully meet the requirement of system.

**4.1.3 The Structure and Fabrication of Delta Robot.** With the limitation of the power, the aim of designing this delta robot is to minimize the size of it. In this article, the delta robot is designed to have a cubical workspace of side 3 mm. To ensure that the joints on each branch are equally spaced, every link in the core structure manufactured by 3D print is connected by the sacrificial tabs. So, first, we put the core structure as the bottom layer (3D

print resin), and then put the middle layer (flexible polyimide) on it. After putting the top layer (3D print resin), the final step is to cut the sacrificial tabs [34]. Here, its base stage radius is  $R = 10$  mm. Effector stage radius is  $r = 2$  mm. Two linkages are  $L_1 = 20$  mm and  $L_2 = 30$  mm. We choose 1 mm as the thickness of the rigid layer. In the real robot, we added two screws to each joint to assist the fixation.

Because of the flexible linkages, the two vertical rotational axes of the approximated universal joint exist the  $D_a$  ( $D_a = 2$  mm) as Fig. 7 shows, which will influence the workspace. Besides, the limitation of the rotational axes should be considered. Regarding the  $\alpha_1$  and  $\alpha_2$  shown by Fig. 7, the range of motion of the rotational axes is limited from  $-90$  deg to  $90$  deg. The limitation of  $\alpha_1$  and  $\alpha_2$  makes the bottom half of the workspace unreachable, and the mainly reachable points are gathered at the top of the workspace.

When calculating the inverse kinematics of delta robot, we define  $O$  as the center of base stage and  $P$  as the center of output stage. We let the rotational axes combined with the base stage as  $A_i$ , next rotational axes as  $B_i$ , and the one combined with the output stage as  $C_i$ . The length of each linkage is  $OA_i = 10$  mm,  $A_iB_i = L_1 = 20$  mm,  $B_iC_i = L_2 = 24$  mm, and  $C_iP = 10$  mm. After determining the trajectory of the end-effector, to achieve the target motion, the entire trajectory is separated into many small straight lines that can be set as  $\Delta x$ ,  $\Delta y$ ,  $\Delta z$ . Then, the target angles of motors are  $\Delta\theta_{11}$ ,  $\Delta\theta_{21}$ , and

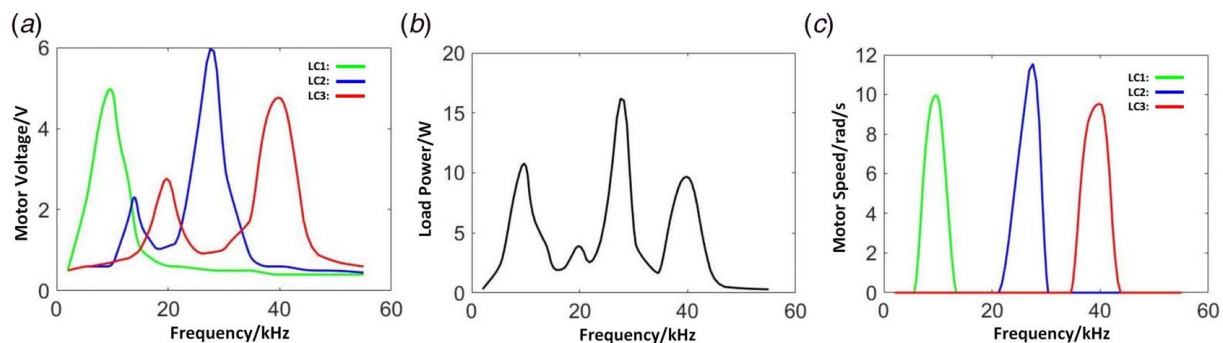


Fig. 4 The validation of the selective frequency characteristic: (a)–(c) the relationship between frequency and motor voltage, load power, and motor speed, respectively

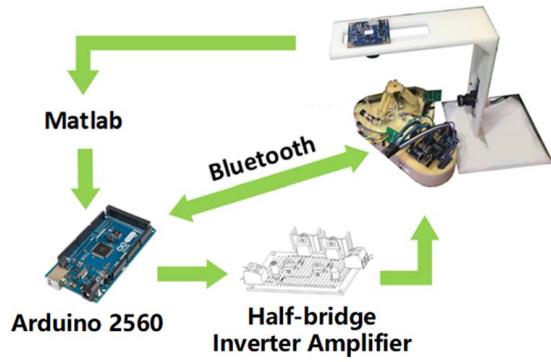


Fig. 5 The overall diagram of the delta robot system based on magnetic coupling resonance

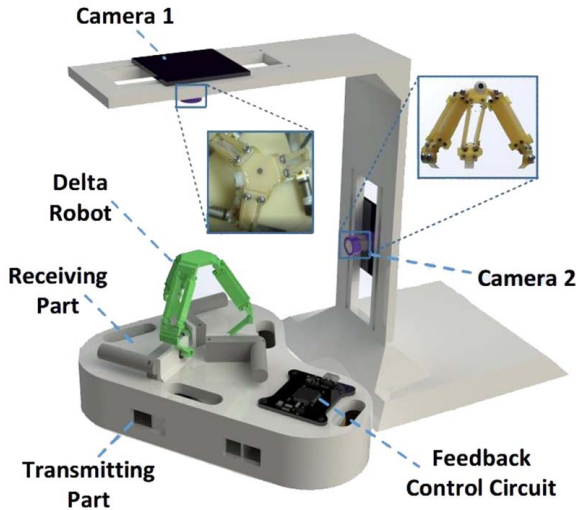


Fig. 6 The overall schematic diagram of the robot system

$\Delta\theta_{31}$ ,  $\angle OA_iB_i$ ,  $\angle A_iB_iC_i$ , and  $\angle B_iC_iP$  are set as  $\theta_{i1}$ ,  $\theta_{i2}$ , and  $\theta_{i3}$ . According to the inverse kinematics of the robot, the relationship between the end-effector output and the motor input is as follows:

$$\mathbf{J}_\theta \begin{bmatrix} \Delta\theta_{11} \\ \Delta\theta_{21} \\ \Delta\theta_{31} \end{bmatrix} = \mathbf{J}_p \begin{bmatrix} \Delta x \\ \Delta y \\ \Delta z \end{bmatrix} \quad (7)$$

where  $\mathbf{J}_\theta$  and  $\mathbf{J}_p$  are the components of Jacobian Matrix in joint space and task space, respectively. Technically, the Jacobian matrix of delta robot is  $\mathbf{J} = \mathbf{J}_\theta \mathbf{J}_p^{-1}$ . Here,

$$\mathbf{J}_p = \begin{bmatrix} J_{1x} & J_{1y} & J_{1z} \\ J_{2x} & J_{2y} & J_{2z} \\ J_{3x} & J_{3y} & J_{3z} \end{bmatrix} \quad (8)$$

where

$$\begin{aligned} J_{1x} &= \sin \theta_{i3} \cos(\theta_{i2} + \theta_{i1}) \cos \gamma_i + \cos \theta_{i3} \sin \gamma_i \\ J_{1y} &= -\sin \theta_{i3} \cos(\theta_{i2} + \theta_{i1}) \sin \gamma_i + \cos \theta_{i3} \cos \gamma_i \\ J_{1z} &= \sin \theta_{i3} \sin(\theta_{i2} + \theta_{i1}) \end{aligned} \quad (9)$$

$$\mathbf{J}_\theta = L_1 \begin{bmatrix} \sin \theta_{12} \sin \theta_{13} & 0 & 0 \\ 0 & \sin \theta_{22} \sin \theta_{23} & 0 \\ 0 & 0 & \sin \theta_{32} \sin \theta_{33} \end{bmatrix} \quad (10)$$

where  $\theta_{i1}$ ,  $\theta_{i2}$ , and  $\theta_{i3}$  are been shown in Fig. 5 and  $\gamma_i$  is the angle between  $OA_i$  and the X axis.

**4.1.4 The Control and Detection System for Delta Robot.** As mentioned in Sec. 2, the discrete input signal and the motor with integrated encoder provide a stage for close-loop control, which can significantly increase the accuracy and reliability of the robot system. As aforementioned, the target position for each motor is  $\Delta\theta_{i1}$ . In addition, aiming to ensure three motors get to the next point at the same time, the interval time between two adjacent points is set to be  $\delta t$ , so the target velocity in each interval is  $\Delta\theta_{i1}/\delta t$ . To realize the double-loop PID control of position and velocity loop, the single-loop control must be achieved first, and then, the two control loops can be nested. For single-loop PID control, we usually use discrete differential equation instead of continuous counterpart. The incremental discrete PID formula is as follows:

$$u(k) = u(k-1) + K_p[e(k) - e(k-1)] + K_i e(k) + K_d[e(k) - 2e(k-1) + e(k-2)] \quad (11)$$

where  $K_p$ ,  $K_i$ , and  $K_d$  are the PID parameters.  $e(k)$  is the current error.  $e(k-1)$  is the error of the last step.  $e(k-2)$  is the error of the last two steps, and  $\gamma_i(k)$  represents the output. In the position loop,  $u(k)$  equals to  $\gamma_i(k)$  and target position  $\Delta\theta_{i1}$  is used to calculate the error, while in the velocity loop,  $u(k)$  represents  $\gamma_{ip}$ , which is the output of the position loop, and target velocity is  $\Delta\theta_{i1}/\delta t$ . In this case, to make the three motors reach every preset position at the same time, a confidence interval is set in each preset position. In other words, a certain overshoot is allowed in this control system, so the derivative parameter is trivial since the main function of it is to reduce the overshoot. Besides, adjusting the three parameters simultaneously is quite difficult, and if the derivative parameter cannot be adjusted properly, it is easy to make the control more unstable. Hence, the incremental PI control is sufficient. Equation (11) can be simplified as follows:

$$u(k) = u(k-1) + K_p[e(k) - e(k-1)] + K_i e(k) \quad (12)$$

Both position loop and velocity loop can be realized by PI controller in single-loop control. When double-loop control is implemented, the two loops need to be nested. The specific diagram is shown in Fig. 8.

The detection method shown in Fig. 6 aims to determine the precision of delta robot. The delta robot was fixed in the center of two orthogonally positioned camera. (The focal length of the camera is 7.6 mm, and the camera frame number is 120 frames per second.) We place two black marker points as track marker of the camera in the center and corner of the delta robot's end-effector. The Camera 1 is for XY-plane track and the Camera 2 is for Z-axis. The real images taken by the two cameras are also shown in Fig. 6. The video captured by the camera is processed by a MATLAB program called multitrack [35], which automatically extracts the position of the marker in each frame of the image. This algorithm can predict the position of markers in the next frame based on the Kalman filter [36] and double exponential smoothing [37], and it is able to label all marker locations in the video automatically.

**4.1.5 The Motion Experiment for the Delta Robot.** In the experiment, three different trajectories are used to verify the performance of device. As mentioned earlier, each trajectories need to be divided into several straight line. Here, the line trajectory includes three dividing points, while square and circle trajectory are divided into eight parts. According to Fig. 9, the trajectory starts from the center point where the thick line represents the theoretical trajectory, and the thin line is the trajectory extracted from the real image captured by the camera. The specific precision is presented in Table. 2. The average precision of line trajectory as low as 1.2 mm is achieved, but the circle trajectory is up to 3.1 mm. There are two main reasons for the error. First, the speed of motor cannot run at a very low speed due to the characteristics of MCR. (At the critical point of MCR, the motor speed increases from 0 to a certain value suddenly. Once the critical point is passed, the speed of the motor can be controlled by controlling the proportion of the corresponding component in the input composite signal.) Therefore, the trajectory cannot be divided into too many small lines, otherwise the time of

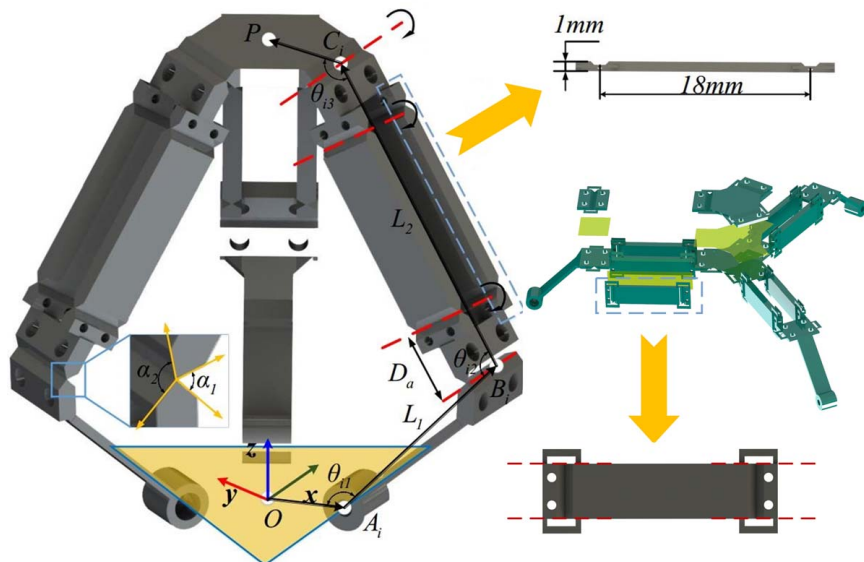


Fig. 7 The fabrication and parameter definition of delta robot

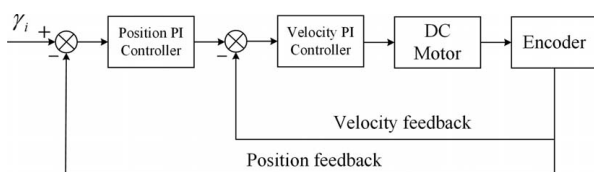


Fig. 8 Control diagram of double-loop control

laminated structure instead of normal linkages with bearings, which may also influence the precision. According to Table 2, the XZ-plane average precision with different trajectory are 1.1 mm, 1.5 mm, and 1.2 mm. Unlike the XY-plane, there is not a big change. So, the accuracy is significantly reduced when taking some relatively complicated trajectories. After processing these two-dimensional data into three dimensions, the total mean error, max error, and mean integral square error (MISE) can be derived and presented in Table 2.

each interval will become very short, which can cause great difficulty to control its accuracy. Second, since the prototype of the delta robot is 3D printed and assembled by hand, the manufacturing and assembly precision cannot be guaranteed, especially in the XY-plane. In addition, to make it smaller, the authors use flexible linkages with

**4.2 Untethered Multi-Actuator Pipe Robot for Sampling Operation.** Frankly speaking, the tethered robot such as the delta robot application cannot be fully benefited from the wireless characteristic of MCR, while the multiplexing control is the key

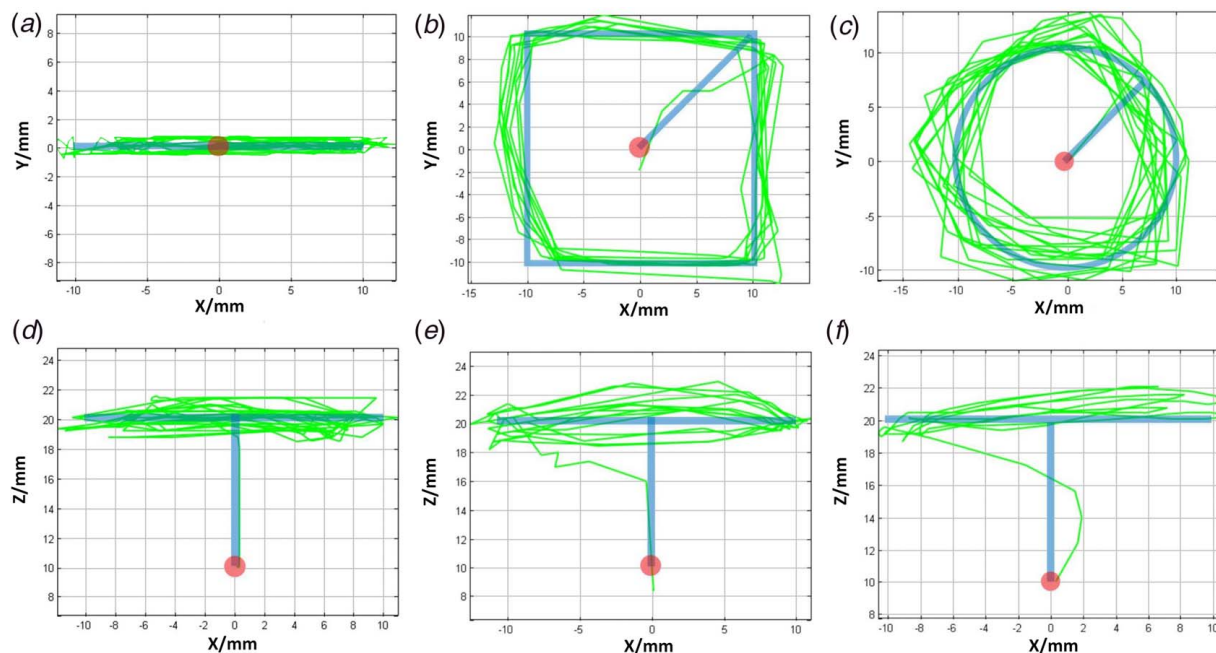
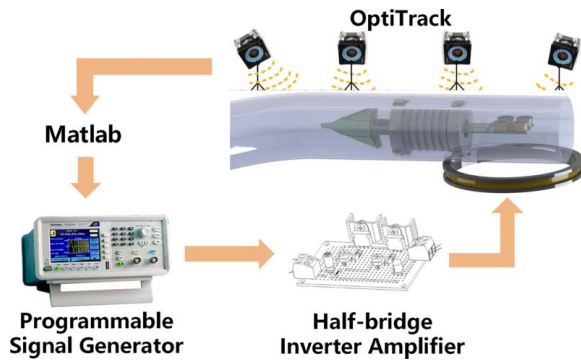


Fig. 9 The comparison between desired trajectory and real trajectory: (a) and (d) the results of line trajectory; (b) and (e) the results of square trajectory; and (c) and (f) the results of circle trajectory



**Table 2 The precision of different trajectory**

Trajectory type	XY-plane mean error (mm)	XZ-plane mean error (mm)	Mean error (mm)	Max error (mm)	MISE (mm <sup>2</sup> )
Line	0.38	1.1	1.2	2.0	2.3
Square	1.1	1.5	1.6	3.1	5.5
Circle	2.4	1.2	3.1	5.1	12.7



**Fig. 10 The overall system diagram of pipe robot based on magnetic coupling resonance**

breakthrough. On the contrary, multiplexing control is indeed beneficial for the untethered robot. But more important, the combined wireless power transfer characteristic makes it achieve fully onboard control without any cables, circuits, and batteries, which can achieve miniaturization under without decreasing the number of actuators.

In this article, a pipe detection and sampling operation scenario are created to verify that the method mentioned earlier can be potentially applied to the practical application. A corresponding multi-actuator pipe robot is designed to meet the requirement of this scenario.

**4.2.1 The Overall Scheme of Pipe Robot.** The overall scheme of the experimental system is shown in Fig. 10. In the experiment, a translucent pipe with an inner diameter of 40 mm made by 3D printing is used to simulate the working environment. The half-bridge inverter amplifier is totally the same as the previous application. Except for the camera, the Optitrack Motion Capture (OptiTrack Prime 41 W) is applied to capture the complete motion of the pipe robot.

Because the shape memory alloy (SMA) spring, which can be only controlled as switch, is used as actuator, the feedback control cannot be realized. Thus, the programmable signal generator (Tektronix AFG 3022) is applied as a signal source. This generator can be programmed offline with MATLAB. After determining the input composite signal as “\*.m” file, it can be imported to the generator by replacing its format to “\*.tfw” file by Arbexpress.

**4.2.2 The Structure and Fabrication of Pipe Robot.** In the design process of main structure, the following functions should be considered: first is free movement in the elbow and straight pipe; second is that the end-effector of the robot can collect residues from at least four directions in the pipe; third is that it can be driven by SMA spring. The target pipe in this article is a circular pipe with a diameter of 40 mm, so to realize the function of sampling, a small gripping mechanism driven by SMA spring is also needed. The specific structural design is as follows.

As shown in Fig. 11, the pipeline robot is mainly divided into three parts: gripper part, moving part, and driving part. The whole production adopts 3D printing technology, so its material is resin material.

As for the gripper part, the gripper based on origami mechanism is achieved, which is easy to be driven by SMA spring. Conversely, benefiting from the origami structure, its volume and weight are smaller and lighter than the general gripper. The design and fabrication in this article is derived from an origami gripper proposed by Edmondson et al. [38].

To realize the movement in the pipe, the moving part of the robot adopts the way of peristalsis. Although this kind of motion mode is limited in its efficiency, it can be adapted to various shapes of pipes. Besides, it is also convenient for SMA spring to drive.

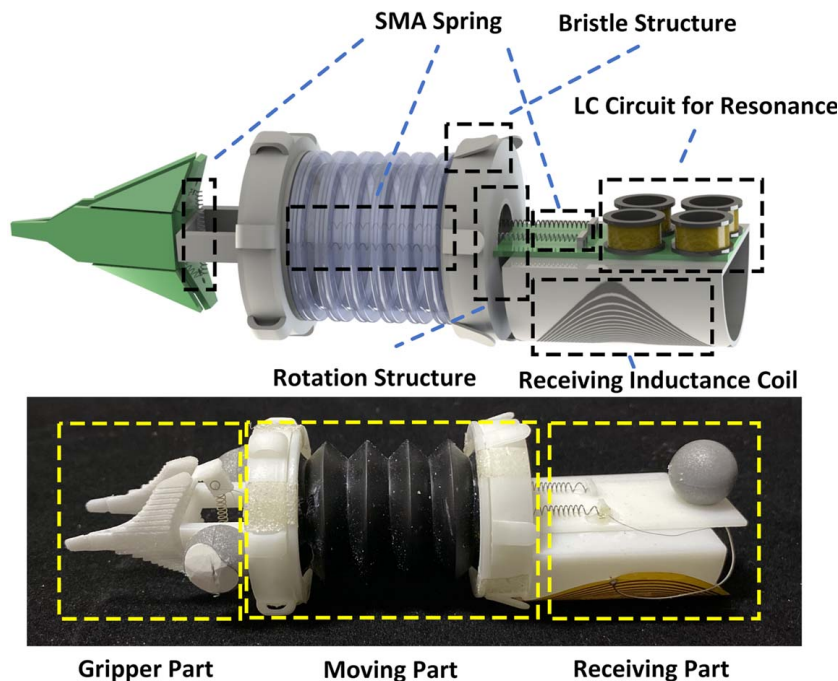


**Fig. 11 The structure diagram of pipe robot**



**Table 3 Circuit parameter table for pipe robot**

Inductance (H)	Capacitance (T)	Resonance (Hz)	Resistance frequency ( $\Omega$ )
$2.21 \times 10^{-5}$	$2.87 \times 10^{-6}$	20,000	0.6
$1.48 \times 10^{-5}$	$1.91 \times 10^{-6}$	30,000	0.6
$1.03 \times 10^{-5}$	$1.17 \times 10^{-6}$	46,000	1.0
$6.56 \times 10^{-6}$	$7.88 \times 10^{-7}$	70,000	1.0

**Table 4 Parameters of SMA spring**

Parameters	One-way SMA	Two-way SMA
High transition temperature ( $^{\circ}\text{C}$ )	—	55
Low transition temperature ( $^{\circ}\text{C}$ )	—	20
Spring wire diameter (mm)/outer diameter (mm)	0.203/1.37	0.300/1.50
Resistance on straight wire ( $\Omega/\text{m}$ )	29.13	25.13
Heating pull force (g)	39.3	56.3
Cooling deformation force (g)	15.94	30.46
Approximate current for 2 s contraction (A)	0.7	0.9
Cooling time (s)	3.0	4.1

The middle of the moving part is a cavity covered by bellows where there are two independent two-way SMA springs. When two springs contract and expand at the same time, the robot can move forward. When only one spring is driven, the gripper will incline to one side, so as to complete the operation of grasping the residues.

The two ends of the moving part are used as supports. The diameter of the left support structure is equal to the inner diameter of the pipe, while the right one imitates the bristle structure of insects, whose overall diameter is slightly larger than the inner diameter. When the moving cavity of the robot contracts, since the moving direction is along the bristle direction, the friction force between the right end support and the pipe is basically the same as that of the left one, it can basically achieve synchronous contraction. When the moving cavity expands, because the moving direction of the right end supports is against the bristle direction, the

friction force of the right side is greater than the left, so the robot can move forward a little.

The junction between moving part and receiving part is a steering mechanism. One passive spring and one active spring are used to achieve the rotation of moving part through cable mechanism. When the moving part rotates, the gripper, which originally moves up and down, can move left and right, because the position of the two springs inside bellows changes from vertical to parallel to the horizontal plane.

The receiving part includes a receiving inductance coil and a LC circuit for resonance. The receiving inductance coil is made of flexible PCB, so it fits perfectly on the outside of the cylinder. The LC circuit is hidden in the cylinder in the final version of robot to provide space for Optitrack target ball. All of the actuators and circuit are connected with 0.1 mm platinum wire.

As for the fabrication, all parts of the robot are made by 3D printing, but the materials of each part are different. Because the origami structure requires higher toughness and strength, the material of gripper is nylon. Due to the bellows needing to be contracted, it is manufactured by 3D printing rubber, which needs to use resin to print a mold first and then pour the rubber (stiffness is 30) and curing agent into the mold. The rest of the robot is made of resin, which makes the overall weight of the robot less than 50 g.

**4.2.3 The Circuit Parameters for Pipe Robot.** To avoid half and double frequency resonance, 20 kHz, 30 kHz, 46 kHz, and 70 kHz are chosen as the resonance frequency for each actuator. 20 kHz and 46 kHz control the two springs inside the bellows, while the active spring of steering mechanism and the spring of origami gripper are driven by 30 kHz and 70 kHz respectively. Here, the resistance of one-way SMA spring is  $0.6\Omega$ , and the two-way spring is  $1\Omega$ . According to these known parameters and the dimensions of the robot, based on the optimization algorithm aforementioned, the following parameters presented in Table 3 can be obtained. As for SMA springs, the parameters of two different types are provided in Table 4.

**4.2.4 The Motion Experiment for Pipe Robot.** First, it is necessary to verify the characteristics of each actuator before the final experiment. In addition, it can also verify the frequency selection characteristics of the control system.

According to the principle proved earlier, when the input signal has only one frequency component, only one spring should be

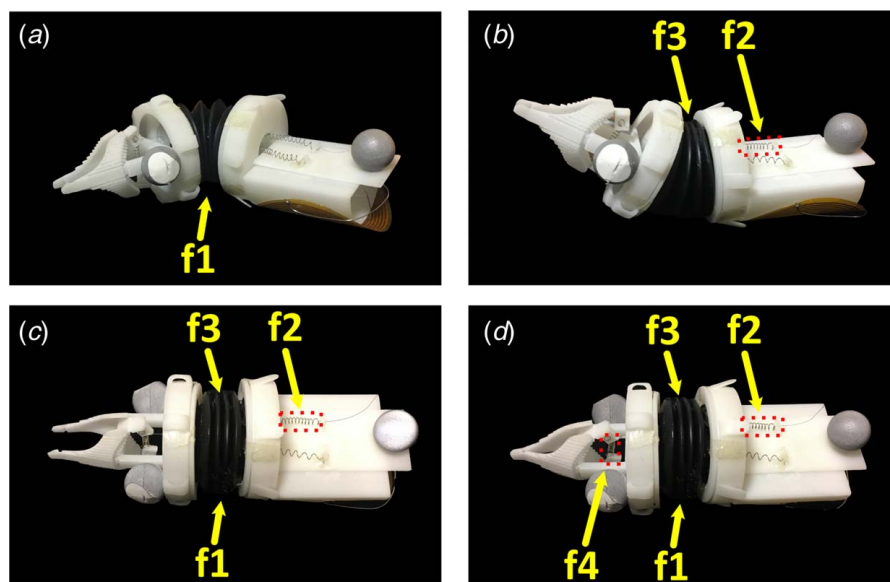


**Fig. 12 The verification experiment for selective frequency characteristic of control system and SMA actuators**

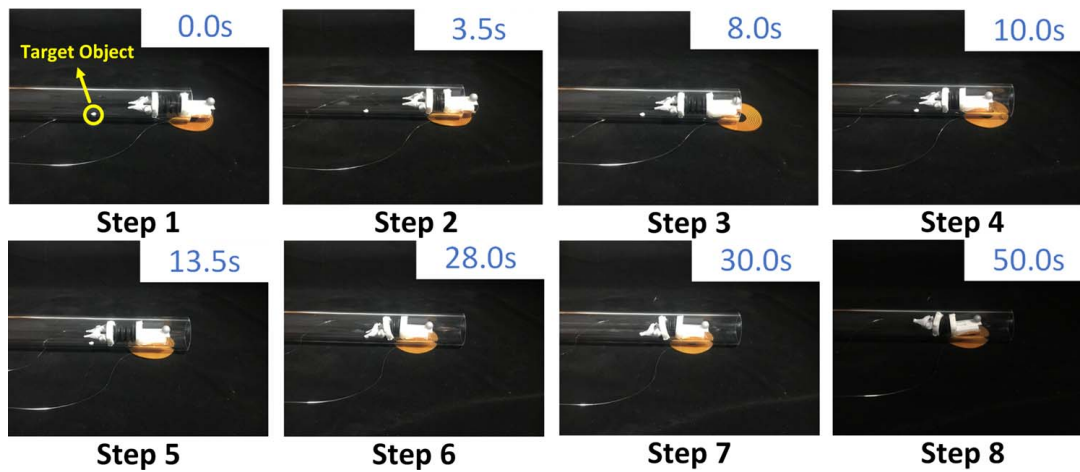


Fig. 13 The process of motion experiment and its corresponding motion time

actuated. Similarly, when the input signal has  $n$  frequency components, its corresponding  $n$  springs are driven. Therefore, to verify the motion effect of each drive, 20 kHz square wave; 30 kHz and 46 kHz square waves; 20 kHz, 30 kHz, and 46 kHz square waves; and four frequency square waves are input, respectively.

As shown in Fig. 12, when the input signal has only 20kHz component, after 1.4 s, the robot reached the pose shown in Fig. 12(a). At this time, only the SMA spring on the left side of the bellows contracted, while the other spring is free. Then, the composite signal of 30 kHz and 46 kHz is input, after 2.1 s, the robot reached the following Fig. 12(b). At this time, the 46 kHz frequency component driven the active spring of the steering mechanism to rotate 90 deg, and the 30 kHz component actuated the spring above the bellows to contract. Here, the gripper part bent upward. When the composite signal of 30 kHz and 46 kHz is added with the frequency component of 20 kHz, after 1.2 s, the robot moved to the pose shown in Fig. 12(c). At this time, two springs inside the bellows are in the state of contraction and the same as the active spring of steering mechanism. When the 70 kHz component is added into the input signal finally, after 1.0 s, the spring of the origami gripper actuated the front structure to close, which proved its grasping ability.

In the final experiment, a residue is set in the pipeline to verify the robot's multi degree-of-freedom motion and grasping ability. The following is the design of the experimental process. First, after putting the wireless robot into the pipeline, the transmitting signal drives the robot to move forward for 50 mm first. Then, it is bend down and the gripper is actuated to grasp the object. After that, the steering mechanism turns the gripper part by 90 deg and drives the robot to bend to the left. Finally, the input signal is stopped to let the robot return to its original state.

The movement process of the robot recorded by the camera is shown in Fig. 13. Each picture indicates the time from the beginning of the movement in the upper right corner. In the first step, at 0.0 s, the signal generator starts to input composite signal. In 3.5 s, the first contraction of two SMA springs in the bellows is completed, and then the robot moves to the sixth step after multiple rounds of contraction and extension. At this time, the robot has arrived near the object to be grasped. Because the system adopts open-loop control, after many attempts, the robot bends down at 28 s when the object is just within the grasp range of the gripper. As shown in Fig. 13 step 7, the one-way SMA spring on the gripper contracts. After 2 s, the object is grasped. After that, the springs in the bellows return to its original state and the active spring of the steering mechanism contracts, making the gripper and moving part rotate at 90 deg. The final step of bending to the right is completed at about 50 s. It can be seen that the pipe robot completes the preset motion experiment, which prove the feasibility

of the control and drive system proposed before and the structural design of the pipe robot.

## 5 Conclusion and Discussion

In this article, the proposed wireless multiplexing control system achieved to drive multiple actuators of robot simultaneously with only one input, which realized the miniaturization and lightweight of the robot structure. Based on the discrete composite signal, the closed-loop control is achieved, which brings the accuracy for this control method first compared with relevant research. Besides, a mathematical model and a corresponding parameter optimization method are first proposed in the light of robotic application. In parameter optimization, five parameters to be optimized are selected in accordance with the actual design requirements. PSO algorithm is implemented due to its fast convergence speed and is less affected by the dimension. The application of delta robot with flexible linkage validated that the wireless multiplexing control can achieve accurate multiple degree-of-freedom motion of a single platform with feedback, while the application of untethered pipe robot proved different motion forms including linear locomotion, bending, rotating, and grabbing can be achieved simultaneously and independently to finish a certain assignment by only one input. Compared with relevant researches that only realize primary function by switch control without feedback, the work shown in this article shows a great improvement in this field.

However, in current applications, although closed-loop control for advanced robot system is achieved, actually there are only three to four actuators that can be driven simultaneously. As for the end-goal application, programmable surface, and artificial skin, the number of actuators that can be driven simultaneously should be increased to at least 16 ( $4 \times 4$ ). Conversely, compared to another WPT method based on electromagnetic induction, MCR possesses much longer transmission distance, and it is also not very sensitive to the distance. Thus, for controlling some actuators that only have two status, such as SMA, energy can be transmitted within a quite large range, not a specific value or have to be very close to the transmitting coil. However, for wider application environments, the distance limitation still cannot be ignored. Hence, further research that relates to keeping the transmission energy stable in a wide distance range is needed.

## Acknowledgment

This research work was supported in part by the National Key Research and Development program of China (Grant No.

## Conflict of Interest

There are no conflicts of interest.

## Data Availability Statement

The datasets generated and supporting the findings of this article are obtainable from the corresponding author upon reasonable request. The authors attest that all data for this study are included in the paper.

## References

- [1] McClintock, H., Temel, F. Z., Doshi, N., Koh, J.-s., and Wood, R. J., 2018, "The Millidelta: A High-Bandwidth, High-Precision, Millimeter-Scale Delta Robot," *Science Robotics*, **3**(14), p. eaar3018.
- [2] Follmer, S., Leithinger, D., Olwal, A., Hogge, A., and Ishii, H., 2013, "inFORM: Dynamic Physical Affordances and Constraints Through Shape and Object Actuation," The ACM Symposium on User Interface Software and Technology (UIST), St. Andrews, UK, Oct. 8–11, Vol. 13, IEEE, p. 2501988.
- [3] Leithinger, D., and Ishii, H., 2010, "Relief: A Scalable Actuated Shape Display," Proceedings of the 4th International Conference on Tangible and Embedded Interaction 2010, Cambridge, MA, Jan. 24–27, ACM.
- [4] Yesin, K. B., Vollmers, K., and Nelson, B. J., 2006, "Modeling and Control of Untethered Biomicrobots in a Fluidic Environment Using Electromagnetic Fields," *Int. J. Rob. Res.*, **25**(5–6), pp. 527–536.
- [5] Zhang, L., Abbott, J. J., Dong, L., Kratochvil, B. E., Bell, D., and Nelson, B. J., 2009, "Artificial Bacterial Flagella: Fabrication and Magnetic Control," *Appl. Phys. Lett.*, **94**(6), p. 064107.
- [6] Troisi, C. S., Knaflitz, M., Olivetti, E. S., Martino, L., and Durin, G., 2008, "Fabrication of New Magnetic Micro-Machines for Minimally Invasive Surgery," *IEEE Trans. Magn.*, **44**(11), pp. 4488–4491.
- [7] Sudo, S., Segawa, S., and Honda, T., 2006, "Magnetic Swimming Mechanism in a Viscous Liquid," *J. Intel. Mater. Syst. Struct.*, **17**(8–9), pp. 729–736.
- [8] Guo, S., Pan, Q., and Khamesee, M. B., 2008, "Development of a Novel Type of Microrobot for Biomedical Application," *Microsyst. Tech.*, **14**(3), pp. 307–314.
- [9] Johnson, B. V., Chowdhury, S., and Cappelleri, D. J., 2020, "Local Magnetic Field Design and Characterization for Independent Closed-Loop Control of Multiple Mobile Microrobots," *IEEE/ASME Trans. Mech.*, **25**(2), pp. 526–534.
- [10] Kurs, A., Karalis, A., Moffatt, R., Joannopoulos, J. D., Fisher, P., and Soljačić, M., 2007, "Wireless Power Transfer Via Strongly Coupled Magnetic Resonances," *Science*, **317**(5834), pp. 83–86.
- [11] Kratochvil, B. E., Frutiger, D., Vollmers, K., and Nelson, B. J., 2009, "Visual Servoing and Characterization of Resonant Magnetic Actuators for Decoupled Locomotion of Multiple Untethered Mobile Microrobots," 2009 IEEE International Conference on Robotics and Automation, Kobe, Japan, May 12–17, IEEE, pp. 1010–1015.
- [12] Frutiger, D. R., Vollmers, K., Kratochvil, B. E., and Nelson, B. J., 2010, "Small, Fast, and Under Control: Wireless Resonant Magnetic Micro-Agents," *Int. J. Rob. Res.*, **29**(5), pp. 613–636.
- [13] Nagy, Z., Frutiger, D. R., Leine, R. I., Glocker, C., and Nelson, B. J., 2010, "Modeling and Analysis of Wireless Resonant Magnetic Microactuators," 2010 IEEE International Conference on Robotics and Automation, Anchorage, AK, May 3–8, IEEE, pp. 1598–1603.
- [14] Xu, K., and Liu, G., 2013, "Design of Selectively Controllable Micro Actuators Powered by Remote Resonant Magnetic Fields," International Conference on Intelligent Robotics and Applications, Busan, South Korea, Sept. 25–28, Springer, pp. 143–154.
- [15] Tung, H.-W., Maffioli, M., Frutiger, D. R., Sivaraman, K. M., Pané, S., and Nelson, B. J., 2013, "Polymer-Based Wireless Resonant Magnetic Microrobots," *IEEE Trans. Rob.*, **30**(1), pp. 26–32.
- [16] Wang, J., Chen, G., and Wang, H., 2019, "Wireless Power and Simo Control Based on Magnetic Coupling Resonance Using in Delta Robot," International Design Engineering Technical Conferences and Computers and Information in Engineering Conference, Anaheim, CA, Aug. 17–23, Vol. 59247, American Society of Mechanical Engineers, p. V05BT07A003.
- [17] Ali, M. M., and Takahata, K., 2011, "Wireless Microfluidic Control With Integrated Shape-Memory-Alloy Actuators Operated by Field Frequency Modulation," *J. Micromech. Microeng.*, **21**(7), p. 075005.
- [18] Nafea, M., AbuZaiter, A., Kazi, S., and Ali, M. S. M., 2017, "Frequency-Controlled Wireless Passive Thermopneumatic Micromixer," *J. Microelectromech. Syst.*, **26**(3), pp. 691–703.
- [19] Zainal, M., Ahmad, A., and Ali, M. M., 2017, "Frequency-Controlled Wireless Shape Memory Polymer Microactuator for Drug Delivery Application," *Biomed. Microdevices*, **19**(1), p. 8.
- [20] Boyvat, M., Vogt, D. M., and Wood, R. J., 2019, "Ultrastrong and High-Stroke Wireless Soft Actuators Through Liquid–Gas Phase Change," *Adv. Mater. Tech.*, **4**(2), p. 1800381.
- [21] Ho, S., Wang, J., Fu, W., and Sun, M., 2011, "A Comparative Study Between Novel Witricity and Traditional Inductive Magnetic Coupling in Wireless Charging," *IEEE Trans. Magn.*, **47**(5), pp. 1522–1525.
- [22] Cannon, B. L., Hoburg, J. F., Stancil, D. D., and Goldstein, S. C., 2009, "Magnetic Resonant Coupling as a Potential Means for Wireless Power Transfer to Multiple Small Receivers," *IEEE Trans. Power Electron.*, **24**(7), pp. 1819–1825.
- [23] Mc Caffrey, C., Umedachi, T., Jiang, W., Sasatani, T., Narusue, Y., Niiyama, R., and Kawahara, Y., 2020, "Continuum Microbot Caterpillar With Wirelessly Powered Shape Memory Alloy Actuators," *Soft Rob.*, **7**(6), p. 0090.
- [24] Boyvat, M., Hafner, C., and Leuthold, J., 2014, "Wireless Control and Selection of Forces and Torques-Towards Wireless Engines," *Sci. Rep.*, **4**(1), p. 5681.
- [25] Boyvat, M., Koh, J.-S., and Wood, R. J., 2017, "Addressable Wireless Actuation for Multijoint Folding Robots and Devices," *Sci. Rob.*, **2**(8), p. eaan1544.
- [26] Yu, X., Xie, Z., Yu, Y., Lee, J., Vazquez-Guardado, A., Luan, H., Ruban, J., Ning, X., Akhtar, A., Li, D., Ji, B., Liu, Y., Sun, R., Cao, J., Huo, Q., Zhong, Y., Lee, C., Kim, S., Gutruf, P., Zhang, C., Xue, Y., Guo, Q., Chempakasseril, A., Tian, P., Lu, W., Jeong, J., Yu, Y., Corrao, J., Tan, C., Kim, B., Lee, K., Feng, X., Huang, X., and Rogers, J., 2019, "Skin-Integrated Wireless Haptic Interfaces for Virtual and Augmented Reality," *Nature*, **575**(7783), pp. 473–479.
- [27] Park, J., Tak, Y., Kim, Y., Kim, Y., and Nam, S., 2011, "Investigation of Adaptive Matching Methods for Near-Field Wireless Power Transfer," *IEEE Trans. Antennas Propagation*, **59**(5), pp. 1769–1773.
- [28] Valtchev, S., Borges, B., Brandisky, K., and Klaassens, J. B., 2009, "Resonant Contactless Energy Transfer With Improved Efficiency," *IEEE Trans. Power Electron.*, **24**(3), pp. 685–699.
- [29] Yuan, Q., Chen, Q., Li, L., and Sawaya, K., 2010, "Numerical Analysis on Transmission Efficiency of Evanescent Resonant Coupling Wireless Power Transfer System," *IEEE Trans. Antennas Propagation*, **58**(5), pp. 1751–1758.
- [30] Sample, A. P., Meyer, D. T., and Smith, J. R., 2010, "Analysis, Experimental Results, and Range Adaptation of Magnetically Coupled Resonators for Wireless Power Transfer," *IEEE Trans. Ind. Electron.*, **58**(2), pp. 544–554.
- [31] Guoqing, H., 2015, "Discussing the Mutual Inductance and the Coupling Coefficient Between Circular Coils," *J. Weinan Normal Univ.*, **30**(14), pp. 24–29.
- [32] Eberhart, R., and Kennedy, J., 1995, "Particle Swarm Optimization," Proceedings of the IEEE International Conference on Neural Networks, Perth, Western Australia, Nov. 27–Dec. 1, Vol. 2, pp. 1942–1948.
- [33] Kalafat, M. A., Sevinç, H., Samankan, S., Altunkaynak, A., and Temel, Z., 2021, "A Novel Origami-Inspired Delta Mechanism With Flat Parallelogram Joints," *ASME J. Mech. Rob.*, **13**(2), p. 021005.
- [34] Correa, J. E., Toombs, J., Toombs, N., and Ferreira, P. M., 2016, "Laminated Micro-Machine: Design and Fabrication of a Flexure-Based Delta Robot," *J. Manufact. Process.*, **24**, pp. 370–375.
- [35] Hedrick, T. L., 2008, "Software Techniques for Two- and Three-Dimensional Kinematic Measurements of Biological and Biomimetic Systems," *Bioinspir. Biomim.*, **3**(3), p. 034001.
- [36] Kalman, R. E., 1960, "A New Approach to Linear Filtering and Prediction Problems," *ASME J. Basic Eng.*, **1**(82), pp. 35–45.
- [37] LaViola, J. J., 2003, "Double Exponential Smoothing: An Alternative to Kalman Filter-Based Predictive Tracking," Proceedings of the Workshop on Virtual Environments 2003, Zurich, Switzerland, May 22–23, ACM, pp. 199–206.
- [38] Edmondson, B. J., Bowen, L. A., Grimes, C. L., Magleby, S. P., Howell, L. L., and Bateman, T. C., 2013, "Oriceps: Origami-Inspired Forceps," ASME 2013 Conference on Smart Materials, Adaptive Structures and Intelligent Systems, Snowbird, UT, Sept. 16–18, ASME.